

**Cite this article as:** Xia Lidong, Huo Xiaojie, Chen Hao, et al. Experimental and Theoretical Analysis of Void Evolution During Irradiation in 0.29V-0.09Ta RAFM Steel[J]. Rare Metal Materials and Engineering, 2021, 50 (04):1139-1145.

# Experimental and Theoretical Analysis of Void Evolution During Irradiation in 0.29V-0.09Ta RAFM Steel

Xia Lidong, Huo Xiaojie, Chen Hao, Yang Zhigang, Zhang Chi

Key Laboratory of Advanced Materials of Ministry of Education, Tsinghua University, Beijing 100084, China

**Abstract:** Helium ion irradiation at 200, 350 and 550 °C was performed on a reduced activation ferritic/martensitic (RAFM) steel to investigate the evolution of voids during irradiation. Experimental results show that radiation damage has a bell-shape distribution along the depth. Both void size and density increase as vacancy production rate increases. When irradiation temperature rises, void size increases and void density decreases. Faceted voids are observed at 550 °C. Void aggregation at grain boundaries (GBs) and void denuded zones (VDZs) are observed at high temperatures. A phase field model was employed to investigate the void evolution mechanism. The simulation results show that the void shape may be attributed to anisotropic void interface energy. During irradiation, as time goes on, void evolution can be divided into three stages: incubation stage, nucleation stage and growth stage.

**Key words:** reduce activation ferritic/martensitic steel; radiation induced voids; phase field; anisotropic interface energy

Reduced activation ferritic/martensitic (RAFM) steels are considered to be one of the promising candidate structure materials for blanket module in fusion nuclear reactors<sup>[1-4]</sup>, for its high thermal conductivity, low swelling, high corrosion resistance, mass productivity and good weldability. Based on the conventional FM heat resist steel, rare metal elements Ta, W are introduced to RAFM steels to replace Nb, Mo, respectively, and other impurity elements including Co, Ni, Cu, Al are strictly restricted to avoid producing long-lived radioactive isotopes in fusion application<sup>[5]</sup>. Addition of refractory metal element Ta to RAFM steels increases the tensile strength at high temperature and resistance to irradiation-induced embrittlement<sup>[6,7]</sup>. Tan et al found that Ta-alloying helps RAFM steel with TMT form ultrafine MX precipitates to gain higher strength at 650 °C without proportional ductility loss, while the Ta/Mn-rich oxide produced in fabrication process can generate dimple, indicating the significant importance of fabrication technique improvement<sup>[8]</sup>. Fatigue life of RAFM steels increased with increasing the Ta content and an optimal content of tungsten at 1.4wt% was suggested concerning fatigue property by Shankar et al<sup>[9,10]</sup>. Micro alloy element Ti replacing Ta in RAFM steels increases the yield strength at room tempera-

ture but degrades quickly to thermal exposure because of larger martensite lath width increase. Ti-Ta interaction accelerates the kinetic of (Ta, Ti)-rich MX phase and exhibits better resistance to aging than single additions<sup>[11,12]</sup>. Rare metal elements and their precipitates are crucial to the performance of RAFM steels.

Atoms of the steels are knocked away from their original lattice sites, which cause large amounts of vacancies under the harsh service environment with high energetic neutron irradiation<sup>[13-15]</sup>. Vacancies aggregate to form voids, which degrade the mechanical properties and lead to dimensional instability<sup>[16-18]</sup>. Therefore, it is essential to have a deeper understanding of the void evolution during irradiation.

Much work has been done to study the void in the past decades. Voids preferably formed at grain boundaries and other interfaces were observed in helium implanted 9Cr martensitic steel at high temperatures<sup>[19]</sup>, while no preferential void formation site was observed at room temperature<sup>[20]</sup>. Void precipitation at dislocation network in Au foil was found<sup>[21]</sup>. Void denuded zones (VDZs) have been observed along the grain boundaries in a Fe15Cr15Ni steel which was irradiated under 18 dpa at 749 K<sup>[22]</sup>. Faceted voids were observed in T91 steel

Received date: April 19, 2020

Foundation item: National Natural Science Foundation of China (51771097); Tsinghua University Initiative Scientific Research Program; National Key Research and Development Plan (2017YFB0305201); Science Challenge Project (TZ2018004)

Corresponding author: Zhang Chi, Ph. D., Professor, School of Materials Science and Engineering, Tsinghua University, Beijing 100084, P. R. China, Tel: 0086-010-62782361, E-mail: [chizhang@tsinghua.edu.cn](mailto:chizhang@tsinghua.edu.cn)

Copyright © 2021, Northwest Institute for Nonferrous Metal Research. Published by Science Press. All rights reserved.

irradiated by 5 MeV  $\text{Fe}^{2+}$  at 460 °C<sup>[15]</sup>. It is also found that void size and density increase as the depth increases<sup>[15]</sup>. However, the former investigations were done separately and the results were based on different materials in diverse irradiation experiment conditions. Therefore, a systematic irradiation experiment on RAFM steel is essential to investigate the effect of temperature, vacancy production rate, irradiation time and material structure on the void evolution during irradiation. A simulation is also needed to acquire a deeper understanding of void evolution mechanism.

In the present work, helium ion irradiation at 200, 350 and 550 °C was performed on a RAFM steel to investigate the evolution of voids during irradiation. A phase field model with anisotropic interface energy was employed to analyze the void evolution mechanism.

## 1 Experiment Procedure

The main composition of the RAFM steel used in this present work is shown in Table 1. Heat treatment on this steel is austenitizing at 1253 K for 45 min first, followed by water quenching and then tempering at 1033 K for 90 min. The helium ion irradiation experiments were conducted at 200, 350 and 550 °C, and the vacuum pressure of irradiation environment is about  $10^{-6}$  Pa. 440 keV helium ions were used in the experiment. During the irradiation experiment, the helium ion scanned beam size was about 20 mm×20 mm and the average beam current was about 5  $\mu\text{A}$ . This set of helium ion irradiation experiment was done on the high energy electron cyclone resonance (ECR) irradiation platform in National Laboratory

of Heavy-ion Accelerators, Lanzhou, China. After irradiation, samples irradiated at different temperatures were observed by transmission electron microscopy (TEM, JEOL 2100) to investigate the void morphology. The TEM samples were obtained by means of focused ion beam (FIB), which is an advanced analytical tool of sample preparation for studies of microstructure of the surface layer. In general, the FIB method for TEM sample preparation includes 4 steps: (1) the deposit of protective materials onto the surface of the selected area; (2) cutting the selected areas; (3) taking the selected area out; (4) reducing the samples' thickness by ion thinning. The procedure is shown in Fig.1.

## 2 Model Description

In order to describe the void evolution in the RAFM steel during irradiation, vacancy concentration  $C_v$  and order parameter  $\eta$  were used.  $C_v = 1$  and  $\eta = 1$  represent the void phase,  $C_v = C_v^{\text{eq}}$  and  $\eta = 0$  represent the matrix steel phase<sup>[23-25]</sup>.  $C_v^{\text{eq}}$  is the equilibrium concentration of vacancy in the steel.

With the Gibbs free energy  $f_m$  and  $f_v$  of matrix steel phase and void phase, respectively, the Gibbs free energy of the system is written as Eq.(1)<sup>[26]</sup>, and the mapping of it is shown in Fig.2.

$$G(C_v, \eta) = [1 - h(\eta)] f_m + h(\eta) f_v + \omega g(\eta) \quad (1)$$

where  $h(\eta)$  is a switching function from 0 to 1,  $g(\eta)$  is a double well potential and  $\omega$  is the height of the double well potential. In the present work, similar to former work,  $h(\eta)$ ,  $g(\eta)$ ,  $f_m$  and  $f_v$  are taken as<sup>[26, 27]</sup>:

$$h(\eta) = 3\eta^2 - 2\eta^3 \quad (2)$$

$$g(\eta) = \eta^2 - 2\eta^3 + \eta^4 \quad (3)$$

$$f_m = \frac{1}{\Omega} \{ C_v E_{\text{formation}}^v + (1 - C_v) G_{\text{Fe}} + k_B T [ C_v \ln C_v + (1 - C_v) \ln (1 - C_v) ] \} \quad (4)$$

Table 1 Main composition of the RAFM steel (wt%)

C	W	V	Mn	Ta	Cr	Fe
0.10	1.50	0.29	0.88	0.09	8.6	Bal.

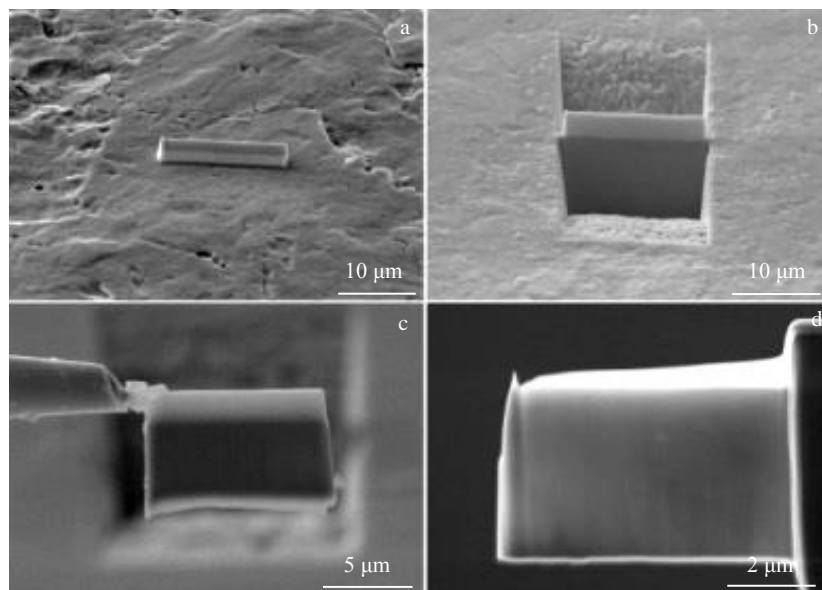


Fig.1 FIB method for TEM sample preparation: (a) protective material deposit, (b) cutting, (c) taking out, and (d) thinning

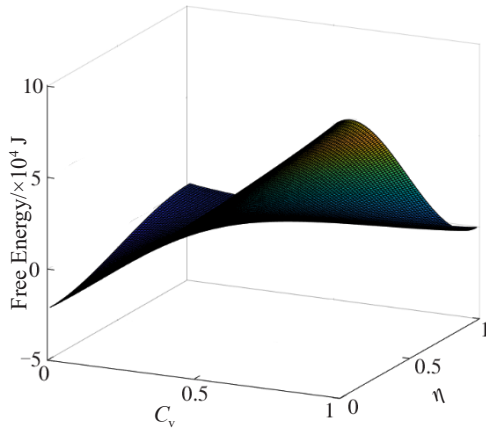


Fig.2 Mapping of the Gibbs free energy of the system (two minima at  $(C_v=1, \eta=1)$  and  $(C_v=C_v^{eq}, \eta=0)$  correspond to the void phase and matrix phase, respectively)

$$f_v = \frac{1}{\Omega} \left\{ C_v E_{\text{sublimation}}^{\text{Fe}} + k_B T [C_v \ln C_v + (1 - C_v) \ln (1 - C_v)] \right\} \quad (5)$$

where  $\Omega$  is the atomic volume,  $E_{\text{formation}}^v$  is the vacancy formation energy,  $E_{\text{sublimation}}^{\text{Fe}}$  is the iron sublimation energy,  $T$  is the absolute temperature and  $k_B$  is the Boltzmann's constant. The total Gibbs free energy  $F(C_v, \eta)$  of the system includes free energy of the two phases and interfacial energy. It is written as:

$$F(C_v, \eta) = \int_V \left[ G(C_v, \eta) + \frac{\kappa^2(\theta)}{2} |\nabla \eta|^2 \right] dV \quad (6)$$

where  $\kappa(\theta)$  is a gradient coefficient associated with the anisotropic interfacial energy, and  $\theta$  is the interface orientation angle, which is defined between the normal direction of the void interface and  $x$ -axis, and is given by  $\theta = \arccos(\eta_x / \sqrt{\eta_x^2 + \eta_y^2})$ , where  $\eta_x$  and  $\eta_y$  are the derivative of  $\eta$  with respect to  $x$  and  $y$ , respectively. An orientation function is used<sup>[28]</sup> to reproduce the voids:

$$f(\theta) = 1 + |\sin \theta| + |\cos \theta| \quad (7)$$

Such a function can give an equilibrium shape with four facets and rounded corners in Wulff construction. The polar plot of interface energy and corresponding Wulff construction are shown in Fig.3. From the interface energy polar plot, it can

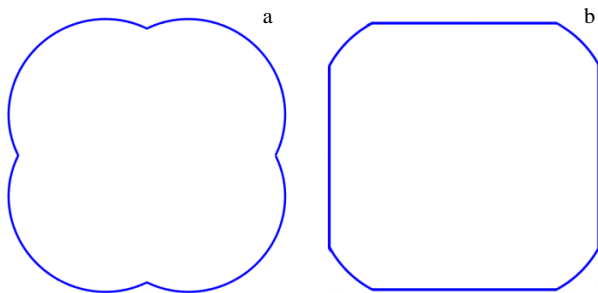


Fig.3 Polar plot of the anisotropic interface free energy (a) and corresponding Wulff construction with four facets and rounded corners (b)

be seen that when  $\theta$  equals  $0^\circ, 90^\circ, 180^\circ, 270^\circ$ , the interface energy is the minimum, and when  $\theta$  equals  $45^\circ, 135^\circ, 225^\circ, 315^\circ$ , the interface energy is the maximum. By the four minimum interface energy values, the equilibrium void shape with four facets and rounded corners is determined through Wulff construction.

The evolution of vacancy concentration  $C_v$  and order parameter  $\eta$  is governed by Cahn-Hilliard equation and Allen-Cahn equation, respectively<sup>[29]</sup>:

$$\frac{\partial C_v}{\partial t} = \nabla \cdot (M \nabla \frac{\delta F}{\delta C_v}) + P_v - R_v - S_v \quad (8)$$

$$\frac{\partial \eta}{\partial t} = -L \frac{\delta F}{\delta \eta} \quad (9)$$

where  $M$  and  $L$  are the mobility coefficient of vacancies and void interfaces, respectively, and  $M=D/k_B T$ , where  $D$  is the diffusivity of vacancies.  $P, R$  and  $S$  are production rate, recombination rate and sink absorption rate of vacancies, respectively.

In the present work, a simplification is performed, where interstitials are not considered, since the main purpose of this research is to demonstrate the effects of interface energy anisotropy on the void morphology evolution during irradiation. Parameters used in the calculation are shown in Table 2. The system size for the simulation is  $128\Delta x \times 128\Delta x$  with grid size  $\Delta x=1$  nm.

### 3 Results and Discussion

The most important parameters controlling the void number density, size and shape during irradiation are temperature, vacancy production rate, irradiated material structure and irradiation time<sup>[13]</sup>. In this irradiation experiment, helium ions have the same kinetic energy, beam current and helium ion scanned area, meaning that the vacancy production rate remains unchanged for all examples.

#### 3.1 Effect of interface energy anisotropy

To research the effect of interface energy anisotropy on void morphology, we firstly investigate the growth of a single void. As shown in Fig.4, a small circular void, whose size is about 20 nm, is put at the centre of the system with supersaturated vacancy concentration. Isotropic interface energy and anisotropic interface energy are used. When isotropic interface energy is used, the initial small circular void grows to a larger circular void, whose size is about 38 nm, as shown in Fig.4b. When anisotropic interface energy is used, void grows to a faceted shape in good agreement with experimental observation at  $550^\circ\text{C}$ , as shown in Fig.5b, so it is reasonable that interface energy anisotropy results in faceted voids during irradiation.

Table 2 Parameters used in the calculation<sup>[27]</sup>

Input parameter	Value
Atomic volume, $\Omega/\text{m}^3$	$1.18 \times 10^{-29}$
Vacancy formation energy, $E_{\text{formation}}^v/\text{eV}$	1.6
Iron sublimation energy, $E_{\text{sublimation}}^{\text{Fe}}/\text{kJ} \cdot \text{mol}^{-1}$	3.5
Void interface energy, $\sigma/\text{J} \cdot \text{m}^{-2}$	2.0
Vacancy diffusivity, $D/\text{m}^2 \cdot \text{s}^{-1}$	$8 \times 10^{-5} \exp\left(\frac{-1.4}{k_B T}\right)$

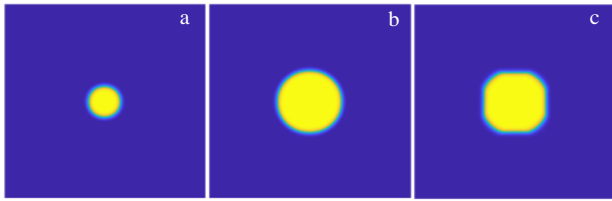


Fig.4 Effect of interface energy anisotropy on the void shape evolution: (a) initial nucleus, (b) isotropic interface energy, and (c) anisotropic interface energy

### 3.2 Effect of irradiation time

Small voids will be absorbed by large voids since vacancies are in a higher energy state around small voids and tend to move to large voids, as shown in Fig.5. During irradiation, the ongoing production of vacancies leads to the formation of a large number of voids. Fig.6 shows the evolution of voids when vacancies are produced continuously. The void evolution can be divided into three characteristic stages, as shown in Fig.7. The first stage is incubation stage, where vacancies are produced continuously and vacancy concentration increases but is not high enough to form stable nuclei<sup>[30]</sup>, so the size is almost zero. As time goes on, the second stage called nucleation stage comes. In this stage, vacancy concentration is high enough so voids nucleate and grow quickly. As a large number of voids form, the absorption rate of vacancies by existing voids increases quickly, and the production rate of vacancies falls behind, which leads to the third stage. In the third growth stage, most of the newly produced vacancies are absorbed by existing voids and few vacancies can form a new nucleus. These already existing voids grow by absorbing vacancies from the system and also by Ostwald ripening, which is at the expense of the smaller ones in large void's vicinity<sup>[31]</sup>. In this stage, as voids become larger, the growth rate slows down.

### 3.3 Effect of vacancy production rate

For the ion irradiation, the irradiation damage varies along the irradiation depth. The irradiation damage profile was simulated by software package SRIM-2013 (Stopping and Range of Ions in Matter) with 40 eV threshold energy for Fe<sup>[32]</sup>. 440 keV helium ions were used in the SRIM-2013 radiation damage calculation. Fig.8 shows that the peak radiation damage is about 2 dpa at the depth of ~900 nm. Above 400 nm underneath the surface, the radiation damage is negligible. From 400 nm, the radiation damage increases quickly and

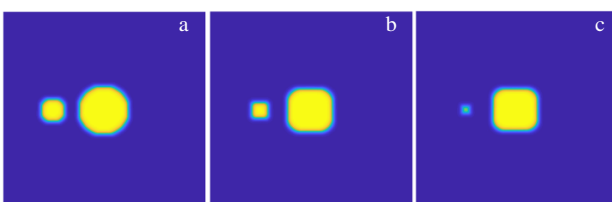


Fig.5 Small voids absorbed by larger voids: (a) initial stage, (b) intermediate stage, and (c) final stage

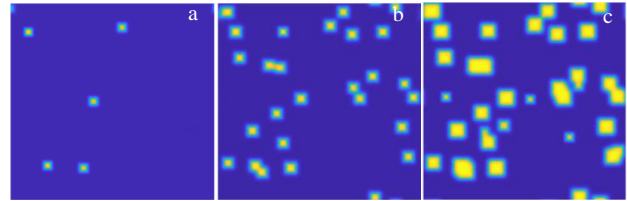


Fig.6 Void evolution with on-going vacancy production: (a) incubation stage, (b) nucleation stage, and (c) growth stage

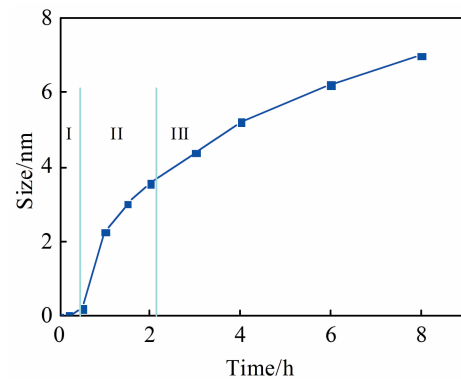


Fig.7 Three characteristic stages of void evolution

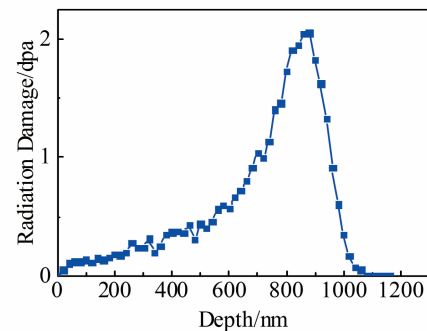


Fig.8 SRIM calculation of radiation displacement damage as a function of depth

reaches the maximum at about 900 nm, and then decreases quickly to zero.

The void micrograph along the irradiation depth is shown in Fig.9a. Within 400 nm underneath the surface, almost no voids can be observed. From 400 nm, voids start to appear, and as depth increases, both void size and density increase with increasing the vacancy production rate. When more vacancies are introduced into the system, more nuclei will form and more vacancies will be absorbed by existing voids<sup>[33]</sup>, leading to rise of both number and size of voids. Void size distribution is shown in Fig.10, which is in good agreement with the irradiation damage profile. A void band is obviously shown in the peak radiation damage region, and the micrograph taken in

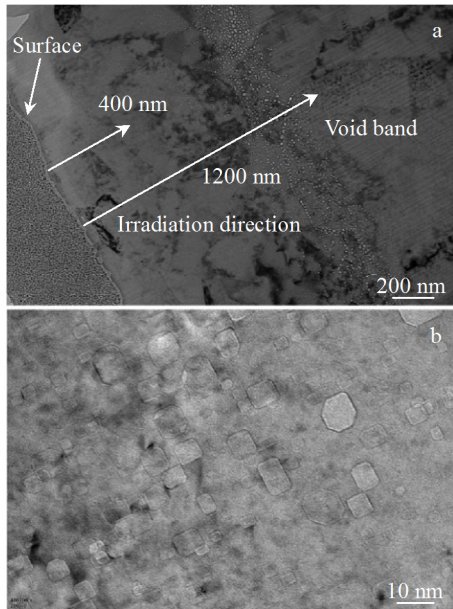


Fig.9 Cross-sectional TEM images of irradiated RAFM steels: (a) whole view from the surface to the irradiated region and (b) faceted voids

this region is shown in Fig.9b. Voids here have a shape of four facets and rounded corners.

### 3.4 Effect of irradiation temperature

TEM micrographs of voids in samples irradiated under 2 dpa at 200, 350 and 550 °C are shown in Fig.11. These micrographs were all taken in the peak radiation damage region,

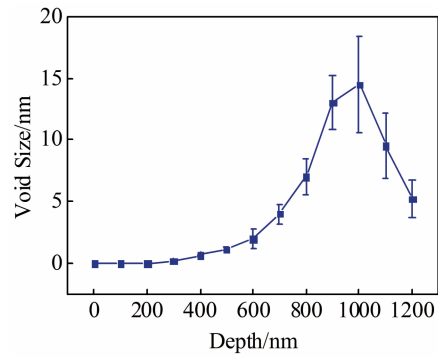


Fig.10 Void size distribution along irradiation depth

which is about 900 nm underneath the surface. As temperatures rise, void size increases and density decreases. The average void diameters at three temperatures are 1.2, 2.3 and 7.1 nm. The average void number densities are  $1.1 \times 10^{25}/\text{m}^3$ ,  $1.5 \times 10^{24}/\text{m}^3$  and  $0.2 \times 10^{24}/\text{m}^3$ . The measured values of void size and density may not be so accurate, because some voids are not very clear in the TEM images due to the TEM image distinguishability. However, the results can reflect the general trend. The rising temperature leads to faster mobility of vacancy and the void interface and thus the voids grow faster and have a larger size. Void density decreases because the rising temperature has two effects<sup>[13,34]</sup>, one is that size voids are absorbed by larger voids known as Ostwald ripening, and the other is that the rising temperature makes vacancies move faster, which means higher recombination rate and lower concentration of vacancy in the system.

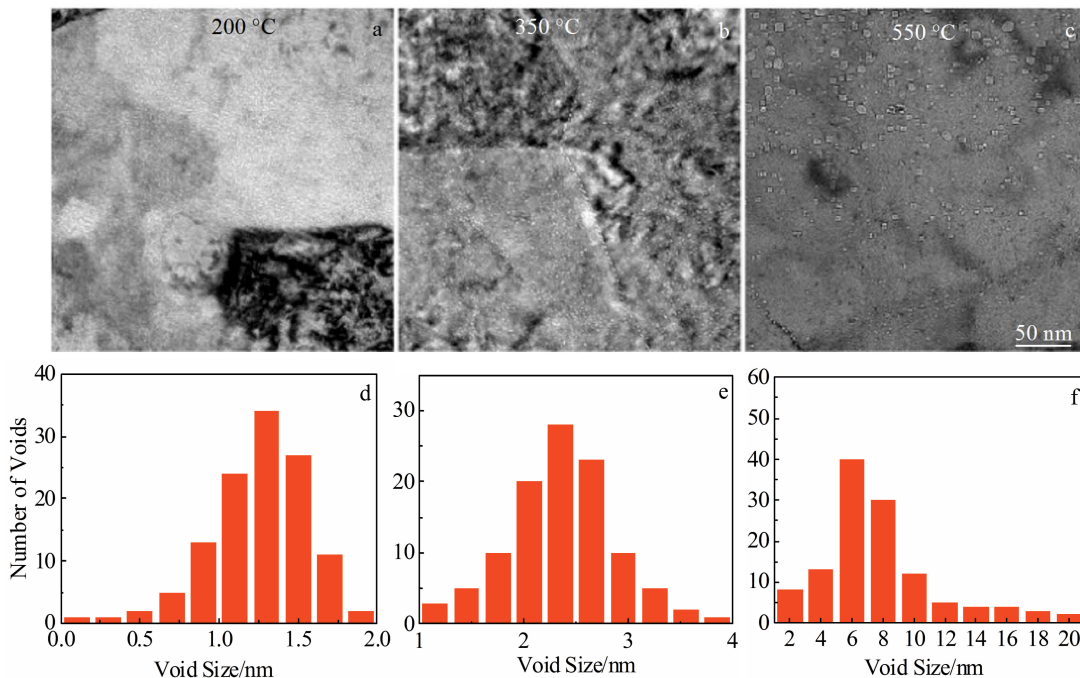


Fig.11 TEM morphologies of voids (a~c) and void size distribution (d~f) at different temperatures: (a, d) 200 °C, (b, e) 350 °C, and (c, f) 500 °C

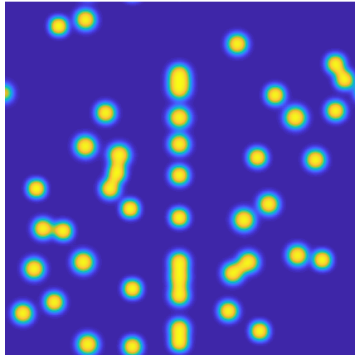


Fig.12 Schematic illustration of aggregation of voids at grain boundaries and VDZs along grain boundaries

### 3.5 Effect of grain boundary

In the above discussion, the effect of grain boundaries is not considered and the void evolution is assumed to take place homogeneously in a perfect lattice matrix. However, grain boundaries play an important role in the process of void evolution<sup>[35]</sup>. Grain boundaries act as strong sinks for mobile vacancies and they compete with existing voids within the grains<sup>[36]</sup>, which reduce the vacancy concentration in grain. In addition, it is easier for voids to nucleate at grain boundaries compared with inner grains due to the lower nucleation energy caused by interfacial effect. Therefore, the premature voids nucleated at grain boundaries will absorb vacancies from the zones nearby, which reduce the vacancy concentration significantly in the zones along grain boundaries. Consequently, void nucleation probability near grain boundaries decreases largely, leading to VDZs along grain boundaries, as shown in Fig.12.

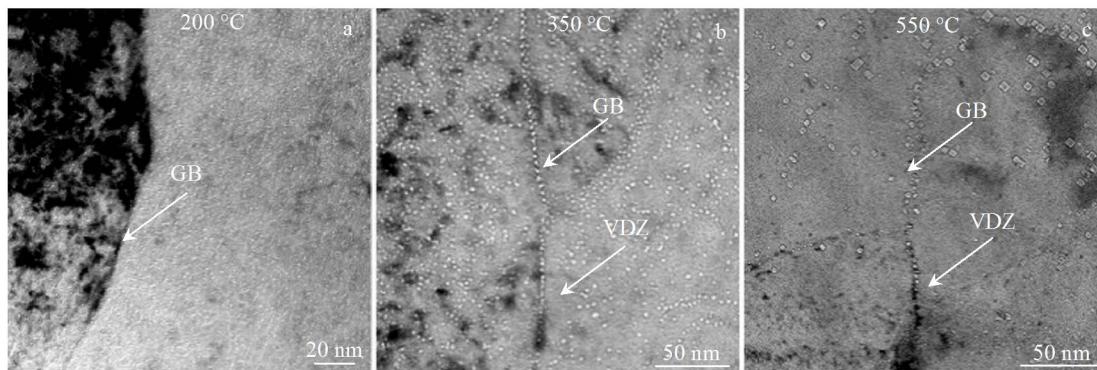


Fig.13 Void morphologies at grain boundary regions: (a) no obvious VDZ at 200 °C, (b) obvious VDZ at 350 °C, and (c) larger VDZ at 550 °C compared to 350 °C

Generally, when temperature is higher, the effect of grain boundaries will play a more important role, due to the faster mobility of vacancies. As shown in Fig.13, VDZs can be observed at 350 and 550 °C, and at 550 °C, it is broader and more obvious; while at 200 °C, obvious VDZs can be hardly observed.

## 4 Conclusions

1) Interface energy anisotropy may lead to the faceted voids with four facets and rounded corners.

2) Void evolution can be divided into three characteristic stages. The first stage is incubation stage, where few voids form and vacancy concentration increases continuously. The second stage is nucleation stage, where a large number of nuclei are formed in a short time. The third stage is growth stage, where most of the newly produced vacancies are absorbed by existing voids and void nucleation rate decreases quickly.

3) Void size and density increase with increasing the vacancy production rate.

4) As irradiation temperature rises, void size increases and density decreases. Faceted voids are obvious at high temperatures, but not at low temperatures.

5) Aggregation of voids at grain boundaries and VDZs along grain boundaries are obvious at high temperatures, but not at low temperatures.

## References

- 1 Yvon P, Carré F. *Journal of Nuclear Materials*[J], 2009, 385(2): 217
- 2 Zinkle Steven J, Busby Jeremy T. *Materials Today*[J], 2009, 12(11): 12
- 3 Klueh R L, Nelson A T. *Journal of Nuclear Materials*[J], 2007, 371(1-3): 37
- 4 PascalYvon, Le Flem Marion, Cabet Céline et al. *Nuclear Engineering and Design*[J], 2015, 294: 161
- 5 Klueh R L, Cheng E T, Grossbeck M L et al. *Journal of Nuclear Materials*[J], 2000, 280(3): 353

- 6 Klueh R L, Alexander D J, Rieth M. *Journal of Nuclear Materials*[J], 1999, 273(2): 146
- 7 Chen Jianguo, Liu Chenxi, Liu Yongchang et al. *Journal of Nuclear Materials*[J], 2016, 479: 295
- 8 Tan L, Yang Y, Busby J T. *Journal of Nuclear Materials*[J], 2013, 442(1-3): 13
- 9 Shankar Vani, Mariappan K, Nagesha A et al. *Fusion Engineering and Design*[J], 2012, 87(4): 318
- 10 Shankar Vani, Mariappan K, Sandhya R et al. *Fusion Engineering and Design*[J], 2015, 100: 314
- 11 Kim Byung Hwan, Jang Jae Hoon, Seol Woo-Kyung et al. *Journal of Nuclear Materials*[J], 2018, 508: 595
- 12 Kim Han Kyu, Lee Ji Won, Moon Joonoh et al. *Journal of Nuclear Materials*[J], 2018, 500: 327
- 13 Trinkaus H, Singh B N. *Journal of Nuclear Materials*[J], 2003, 323(2-3): 229
- 14 Yamamoto T, Odette G R, Miao P et al. *Journal of Nuclear Materials*[J], 2009, 386-388: 338
- 15 Wang Xu, Monterrosa Anthony M, Zhang Feifei et al. *Journal of Nuclear Materials*[J], 2015, 462: 119
- 16 Fu Z Y, Liu P P, Wan F R et al. *Fusion Engineering and Design* [J], 2015, 91: 73
- 17 Gaganidze E, Petersen C, Aktaa J. *Journal of Nuclear Materials*[J], 2009, 386-388: 349
- 18 Klueh R L, Hashimoto N, Sokolov M A et al. *Journal of Nuclear Materials*[J], 2006, 357(1-3): 169
- 19 Henry J, Mathon M H, Jung P. *Journal of Nuclear Materials* [J], 2003, 318: 249
- 20 Jiao Z, Ham N, Was G S. *Journal of Nuclear Materials*[J], 2007, 367-370: 440
- 21 Hetherly J, Martinez E, Di Z F et al. *Scripta Materialia*[J], 2012, 66(1): 17
- 22 Yoshihiro Sekio, Shinichiro Yamashita, Sakaguchi Norihito et al. *Journal of Nuclear Materials*[J], 2015, 458: 355
- 23 Millett Paul C, El-Azab Anter, Rokkam Srujan et al. *Computational Materials Science*[J], 2011, 50(3): 949
- 24 Millett Paul C, El-Azab Anter, Dieter Wolf. *Computational Materials Science*[J], 2011, 50(3): 960
- 25 Hu Shenyang, Burkes Douglas E, Lavender Curt A et al. *Journal of Nuclear Materials*[J], 2016, 479: 202
- 26 Hu S Y, Murray J, Weiland H et al. *Calphad*[J], 2007, 31(2): 303
- 27 Liang Linyun, Lü Guanghong. *Acta Phys Sin Ch Ed*[J], 2013, 62(18): 1
- 28 Liu W B, Wang N, Ji Y Z et al. *Journal of Nuclear Materials* [J], 2016, 479: 316
- 29 Chen L Q, Shen J. *Comput Phys Commun*[J], 1998, 108(2-3): 147
- 30 Millett Paul C, Michael Tonks. *Current Opinion in Solid State and Materials Science*[J], 2011, 15(3): 125
- 31 Srujan Rokkam, El-Azab Anter, Millett Paul et al. *Modeling and Simulation in Materials Science and Engineering*[J], 2009, 17(6): 64 002
- 32 Marquis Emmanuelle A, Hu Rong, Thomas Rousseau. *Journal of Nuclear Materials*[J], 2011, 413(1): 1
- 33 Hu Wenhui, Guo Liping, Chen Jihong et al. *Fusion Engineering and Design*[J], 2014, 89(4): 324
- 34 Was Gary S, Wharry Janelle P, Frisbie Brian et al. *Journal of Nuclear Materials*[J], 2011, 411(1-3): 41
- 35 Millett Paul C, Tonks Michael R, Biner S B et al. *Journal of Nuclear Materials*[J], 2012, 425(1-3): 130
- 36 Liu W B, Zhang J H, Ji Y Z et al. *Journal of Nuclear Materials* [J], 2018, 500: 213

## 0.29V-0.09Ta RAFM 钢辐照条件下空洞演化的实验和理论研究

夏礼栋, 霍晓杰, 陈浩, 杨志刚, 张弛

(清华大学先进材料教育部重点实验室, 北京 100084)

**摘要:** 为研究辐照条件下空洞的演化, 分别在 200, 350 和 550 °C 对低活化铁素体/马氏体钢 (RAFM) 进行 He 离子辐照。实验结果显示, 辐照损伤沿深度呈钟型分布, 空洞的尺寸和密度均与空位产生率正相关。随着辐照温度升高, 空洞的尺寸增大, 密度降低, 高温下可以观察到空洞在晶界的聚集和无空洞区 (VDZs), 在 550 °C 可以观察到方形空洞。使用相场模型模拟空洞的演化机制, 模拟结果显示, 辐照条件下空洞演化可以分为孕育、形核和生长 3 个阶段, 空洞界面能的各项异性是空洞形状的可能原因。

**关键词:** 低活化铁素体马氏体; 辐照空洞; 相场; 界面能各向异性

作者简介: 夏礼栋, 男, 1993 年生, 博士生, 清华大学材料学院, 北京 100084, 电话: 010-62782361, E-mail: steve\_man@163.com